Journal of Controlled Release 194 (2014) 82–91

Contents lists available at ScienceDirect

Journal of Controlled Release

journal homepage: www.elsevier.com/locate/jconrel

Comparison of active, passive and magnetic targeting to tumors of multifunctional paclitaxel/SPIO-loaded nanoparticles for tumor imaging and therapy

Nathalie Schleich [a], Chrystelle Po [b], Damien Jacobs [a,b], Bernard Ucakar [a], Bernard Gallez [b], Fabienne Danhier [a,1], Véronique Préat [a,*,1]

[a] Université Catholique de Louvain, Louvain Drug Research Institute, Advanced Drug Delivery and Biomaterials, Avenue Mounier, B1 73.12, 1200 Brussels, Belgium
[b] Université Catholique de Louvain, Louvain Drug Research Institute, Laboratory of Biomedical Magnetic Resonance, Avenue Mounier, B1 73.08, 1200 Brussels, Belgium

ARTICLE INFO

Article history:
Received 23 May 2014
Accepted 30 July 2014
Available online 29 August 2014

Keywords:
Theranostic
Nanoparticle
Tumor targeting
Paclitaxel
SPIO
MRI

ABSTRACT

Multifunctional nanoparticles combining therapy and imaging have the potential to improve cancer treatment by allowing personalized therapy. Herein, we aimed to compare *in vivo* different strategies in terms of targeting capabilities: (1) passive targeting *via* the EPR effect, (2) active targeting of $\alpha_v\beta_3$ integrin *via* RGD grafting, (3) magnetic targeting *via* a magnet placed on the tumor and (4) the combination of magnetic targeting and active targeting of $\alpha_v\beta_3$ integrin. For a translational approach, PLGA-based nanoparticles loaded with paclitaxel and superparamagnetic iron oxides were used. Electron Spin Resonance spectroscopy and Magnetic Resonance Imaging (MRI) were used to both quantify and visualize the accumulation of multifunctional nanoparticles into the tumors. We demonstrate that compared to untargeted or single targeted nanoparticles, the combination of both active strategy and magnetic targeting drastically enhanced (i) nanoparticle accumulation into the tumor tissue with an 8-fold increase compared to passive targeting (1.12% and 0.135% of the injected dose, respectively), (ii) contrast in MRI (imaging purpose) and (iii) anti-cancer efficacy with a median survival time of 22 days compared to 13 for the passive targeting (therapeutic purpose). Double targeting of nanoparticles to tumors by different mechanisms could be a promising translational approach for the management of therapeutic treatment and personalized therapy.

1. Introduction

Multifunctional nanoparticles combining therapy and imaging have the potential to improve cancer treatment by allowing personalized therapy. Based on the advances made in different scientific disciplines, such as chemistry, biology, pharmacy, nanotechnology, medicine and imaging, many reports have shown that the use of nanotheranostics is one of the most promising methods, although this is still at an early stage [1–3].

Theranostics refers to the combination of a therapeutic and a diagnostic agent in the same unique vector. This term is commonly used to describe a multifunctional system combining therapeutic and imaging abilities [1]. Such a tool could be helpful in non-invasive assessment of the biodistribution, visualization of drug distribution, optimization of strategies, prediction and real-time monitoring of therapeutic responses [1,4].

Additionally, nanotheranostics can be used for preselecting patients, seeming to hold significant potential for personalizing nanomedicine (chemo-) therapeutic interventions. Theranostic strategies range from set-ups in which patients are pre-selected on the basis of initial target site accumulation studies. It is important to note that theranostics takes its place in its broadest sense. Many publications claim that theranostics can be used for simultaneous diagnosis and treatment. The diagnosis purpose of theranostics should not refer to the identification, the localization and/or the staging of tumors but to the pre-selection of patients, to the prediction of potential therapeutic responses, and/or to the longitudinal monitoring of treatment efficacy [5]. The first step toward personalized nanomedicine treatment is to pre-select patients on the basis of non-invasive imaging insights on target site accumulation. A second personalization step consists of the non-invasive monitoring of the response to the first cycles of treatment. During this monitoring, the treatment should be adapted, if necessary [5,6].

Different tumoral targeting strategies have been described in the literature. However, *in vivo* quantification of the accumulation of theranostic nanoparticles targeting tumors by different strategies has not been studied yet [7,8]. Hence, we evaluated *in vivo* in parallel three tumoral targeting strategies.

* Corresponding author. Tel.: +32 2 764 73 09; fax: +32 2 764 73 98.
E-mail address: veronique.preat@uclouvain.be (V. Préat).
[1] These two authors contributed equally.

http://dx.doi.org/10.1016/j.jconrel.2014.07.059
0168-3659/

Passive targeting is based on the so-called enhanced permeability and retention (EPR) effect [9]. This strategy relies on the presence of fenestrations in the endothelium of tumor vessels. These fenestrations allow the entry of macromolecules or nanoparticles into the tumor tissue (enhanced permeability effect). Moreover, the deficiency of the lymphatic system in tumor tissue prevents the recapture of these macromolecules leading to a retention effect [7,9,10].

Active targeting consists of coupling a ligand to the surface of nanoparticles that can interact with its receptor at the target cell site [8,11]. Although angiogenesis is a physiological process by which new blood vessels are formed, it is also at the root of tumor growth and metastasis. Since angiogenesis is controlled by the endothelial cells, it is of great interest to target tumor endothelial cells. $\alpha_v\beta_3$ is an adhesion integrin overexpressed at the surface of the endothelial cells of neo-angiogenic vessels involved in the angiogenic process. Its expression is correlated with the malignancy of tumor. Moreover, $\alpha_v\beta_3$ is also overexpressed at the surface of many tumor cells. Therefore, many efforts have been made by researchers to specifically target this integrin in order to make the most of this "double sword" [11,12]. Numerous studies have shown that the tripeptide arginine–glycine–aspartic acid (RGD) was able to bind preferentially to particular $\alpha_v\beta_3$ integrins [11,13–15].

More recently, *magnetic drug targeting* has been studied. In this approach, magnetic nanoparticles are guided to the tumor site using magnetic fields [16,17].

Many groups have demonstrated differential levels of tumor growth between tumors treated by targeted or untargeted drug-loaded nanoparticles. However, only few have shown *in vivo* efficacy in both therapeutic and diagnostic approaches. We hypothesized that the combination of both active strategy and magnetic targeting could enhance multifunctional nanoparticle concentration into the tumor tissue leading, therefore, to a better anti-cancer efficacy (therapeutic purpose) and increased contrast enhancement in MRI (diagnosis purpose). Our main objective was to directly evaluate different targeting strategies *in vivo* using two complementary techniques: (1) the electron spin resonance (ESR) spectroscopy, a very sensitive quantification tool [18,19] and (2) the 11.7 T magnetic resonance imaging (MRI), a quantification and an imaging tool [20].

The present study relies on previously developed and described nanoparticles [21]. These dual paclitaxel/superparamagnetic iron oxide-loaded PEGylated PLGA-based nanoparticles showed strong magnetic properties, and *in vivo* anti-tumor efficacy. In a view of a translational approach, poly(lactide-co-glycolide) (PLGA) was chosen for its biodegradability properties, its biocompatibility and its approval in parenteral products by the FDA.

Hence, different strategies have been compared in terms of targeting capabilities: (1) passive targeting *via* the EPR effect, (2) active targeting of $\alpha_v\beta_3$ integrin *via* RGD grafting, (3) magnetic targeting *via* a magnet placed on the tumor and (4) the combination of the magnetic targeting and the active targeting of $\alpha_v\beta_3$ integrins (Fig. 1).

We aimed at comparing different targeting strategies for multifunctional nanoparticles in terms of anti-cancer efficacy, biodistribution, and MRI contrast agent efficiency. The most effective targeting strategy was obtained by the use of a combination of active strategy using RGD-grafted nanoparticles and magnetic targeting.

2. Material and methods

2.1. Nanoparticle formulation

Superparamagnetic iron oxides (SPIO) coated with oleic acid were synthetized by a co-precipitation technique of ferrous and ferric salts

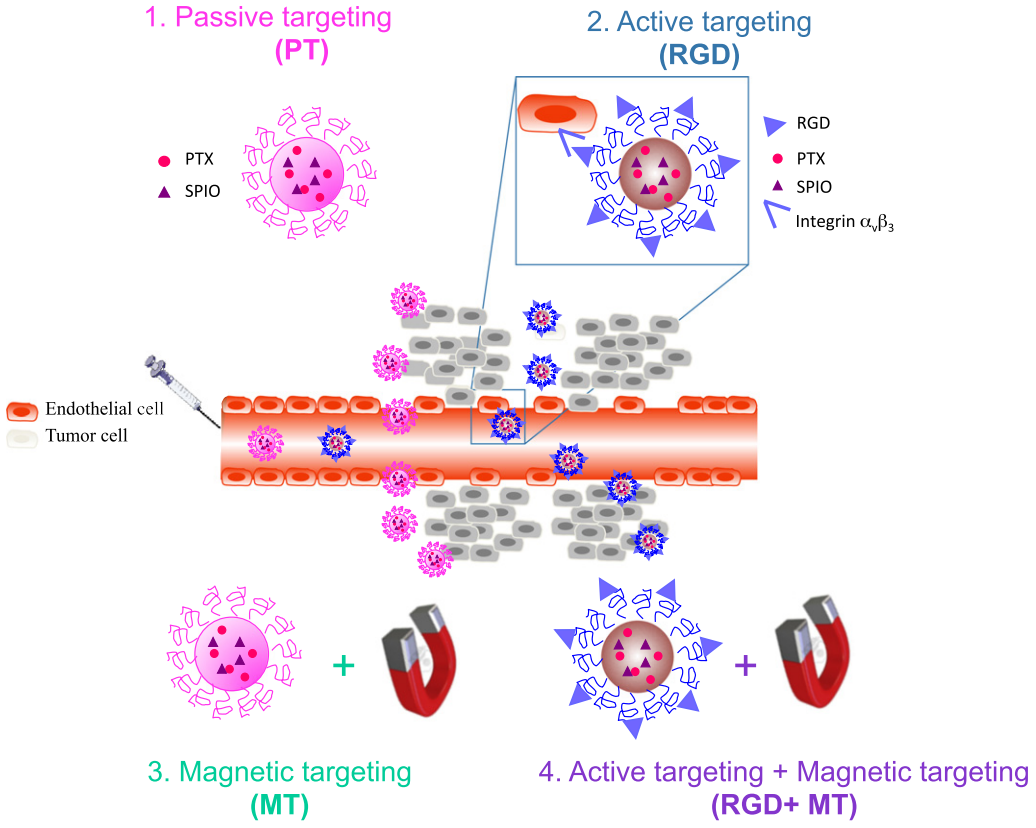

Fig. 1. Schematic representation of the different tumor targeting strategies compared in the present study. (1) Passive targeting *via* the EPR effect (PT), (2) active targeting of $\alpha_v\beta_3$ integrin *via* RGD grafting (RGD), (3) magnetic targeting *via* a magnet of 1.1 T placed on the tumor (MT) and (4) the combination of magnetic targeting and active targeting of $\alpha_v\beta_3$ integrin (RGD + MT).

in alkaline medium as previously described [21]. All nanoparticle formulations were prepared by an emulsion–diffusion–evaporation method [7,21,22]. Briefly, PLGA (Sigma Aldrich, 28 mg/ml), PLGA-PEG (6 mg/ml) and PCL-PEG (6 mg/ml), synthesized as previously described [11,22], were dissolved in 2 ml dichloromethane containing SPIO (30 mg/ml) and paclitaxel (PTX) (Chemieliva) (1.5 mg/ml) [21]. This organic solution was then added to an aqueous solution (4.5 ml) containing 3% (p/v) PVA and emulsified using a vortex for 2 min followed by sonication (2 × 30 s, 50 W). The mixture was then added dropwise and under magnetic stirring into an aqueous solution containing 1% PVA and stirred overnight to evaporate the organic solvent. To remove the non-encapsulated drug and oleic acid-coated SPIO, the suspension was filtered (1.2 μm) and washed three times with water using ultracentrifugation (11,000 g, 30 min, 4 °C) and suspended in 2 ml water. Two different types of nanoparticles were prepared:

(1) SPIO/PTX-loaded nanoparticles (SPIO/PTX-NP)
(2) SPIO/PTX-loaded nanoparticles grafted with the RGD peptide on their surface (SPIO/PTX-NP RGD).

For the latest formulation, we used exactly the same method while PCL-PEG was replaced by PCL-PEG-RGD that was synthetized by photografting as previously described [23].

2.2. Physico-chemical characterization

The *hydrodynamic particle size* and size polydispersity of nanoparticles was assessed using a dynamic light scattering method (Nano ZS, Malvern instruments, UK).

The *Zeta* (ζ) *potential* of the nanoparticles was measured in KCl 1 mM with a Malvern Nano ZS at 25 °C.

Iron content was measured by electron spin resonance (ESR) using a Bruker EMX ESR spectrometer operating at 9 GHz (BrukerBiospinGmBh) validated by inductively coupled plasma mass spectroscopy (ICP-MS) measurements (Agilent 7500ce instrument) [24]. Typical parameters were selected for ESR measurements: 3 mT modulation amplitude, 10.11 mW power, 325.1 mT center field, and 400 mT sweep width field. Double integration of the iron oxides ESR spectra was used to quantify signal intensity.

PTX content was determined using high-performance liquid chromatography (HPLC) with UV detection at 227 nm (Agilent 1100 series, Agilent Technologies), as previously described after dissolution of the particles by acetonitrile [25]. The mobile phase consisted of acetonitrile and water (70:30 v/v, respectively) at the rate of 1 ml/min. The column used was a CC 125/4 Nucleod UR 100-5 C18. The drug loading was defined as the amount of drug (mg) loaded for 100 mg of polymer whereas the encapsulation efficiency was defined by the ratio of the encapsulated drug compared to the initial amount of drug [7,21].

Saturation magnetization values were obtained from the fitting by a theoretical relaxation model of Nuclear Magnetic Relaxation Dispersion (NMRD) profiles recorded at 37 °C on a Fast Field Cycling Relaxometer (Stelar, Mede, Italy) over a magnetic field range from 0.01 to 40 MHz. The proton NMRD curves were fitted using data-processing software, including different theoretical models describing the nuclear relaxation phenomena [21].

2.3. Animal models

All experiments were performed in compliance with guidelines set by national regulations and were approved by the ethical committee for animal care of the medical sector of the Université Catholique de Louvain. CT26 colon carcinoma was chosen because of its sensitivity to PTX [26] and of its angiogenic properties [27]. CT26 colon carcinoma cells were inoculated subcutaneously in the right flank or in the right leg (to avoid respiratory artifacts in MRI studies) of BALB/c mice (5×10^4 cells per mouse) depending on the experiment. For all the experiments, mice were divided into 5 groups:

Group 1: control group (injected with PBS for *in vivo* anti-tumor efficacy study and histological study and SPIO-loaded nanoparticles for *ex vivo* biodistribution and MRI),
Group 2: mice treated by SPIO/PTX-NP (passive targeting, PT),
Group 3: mice treated by SPIO/PTX-NP grafted with RGD peptide (active targeting or RGD),
Group 4: mice treated with SPIO/PTX-NP magnetic guided by placing a 1.1 T neodyme-iron-bore external magnet (Webcraft GmbH) on the surface of the tumor for 1 or 4 h (magnetic targeting or MT),
Group 5: mice treated with SPIO/PTX-NP using both magnetic and active targeting (RGD + MT).

For magnetic targeting, the magnet was placed directly in contact with the tumor surface and fixed by a bandage. The bandage was fixed in the space between the magnet and the skin not exceeding 0.3 cm. The exposure time varied from 1 h (ESR spectroscopy) to 4 h (*in vivo* anti-tumor efficacy, ESR spectroscopy and MRI experiments as well as histological studies).

PTX and Fe doses were 5 mg/kg and 27.1 mg/kg, respectively, for *in vivo* anti-tumor efficacy experiments and 2.5 mg/kg and 13.5 mg/kg for the other experiments. For tumor inoculation, mice were anesthetized by intra-peritoneal injections of a mixed ketamine (100 mg/kg) and xylazine (10 mg/kg). For *in vivo* MRI experiments, mice were maintained under anesthesia during the entire experiment using 1–2% isoflurane (Abbott) inhalation in air.

2.4. In vivo anti-tumor efficacy

The effect of SPIO/PTX-NP on tumor growth was assessed by daily measurements of tumor volume with an electronic caliper. CT26 cells were injected subcutaneously in the right flank of the mice to allow easy and reproducible tumor volume measurements. Mice were randomly assigned to a treatment group when the tumor reached a volume of 27 ± 5 mm^3. Treatments were injected trough the tail vein. Five groups were defined as aforementioned ($n = 6$): PBS, PT, RGD, MT and RGD + MT. In this experiment, the magnet was placed on the surface of the tumor for 4 h. The end point of the experiment was determined as the moment when the tumor reached 600 mm^3. At this point, the mice were sacrificed.

2.5. Ex vivo biodistribution study by ESR spectroscopy

The biodistribution of the different treatments was assessed using ESR spectroscopy (X-band). CT26 cells were subcutaneously inoculated in the right flank of the mice. When the tumor reached 50–100 mm^3 in volume, the mice were randomly dispersed into 5 groups as aforementioned ($n = 6$): CTRL, PT, RGD, MT and RGD + MT. The control group was a group injected with SPIO-loaded nanoparticles. For mice treated with magnetic targeting, the external magnet was maintained on the tumor until sacrifice. Treatments were injected into the tail vein of the mouse. 1 or 4 h post-treatment, a retro-orbital blood sample was taken from the mice and they were then sacrificed for dissection in order to remove the liver, lungs and tumor. Thereafter, samples were frozen in liquid nitrogen, dehydrated for 24 h in a freeze-dryer (Labconco), crushed into a fine powder, weighed and analyzed by ESR spectroscopy to determine iron concentration in each tissue.

2.6. In vivo MR imaging

For these experiments, CT26 cells were injected subcutaneously in the right leg of the mice to avoid respiratory artifacts. Mice were enrolled in the study when tumor reached 50–100 mm^3 in diameter. The same amount of SPIO/PTX-NP or SPIO/PTX-NP-RGD were injected,

and the same groups were defined ($n = 5$): PT, RGD, MT and RGD + MT. Each mouse was imaged before and 1 h after treatment injection into the tail vein in order to use each mouse as its own control.

MR experiments were performed using a 11.7 T Bruker Biospec horizontal MR System (Bruker Biospin). RF transmission and reception were achieved with a quadrature volume resonator (inner diameter 40 mm). At first, the mice were anesthetized by isoflurane inhalation of 3% in air and they were placed in an MRI compatible cradle. The breathing rate was assessed *via* a breathing pillow, placed under the thorax, and kept at 70 breaths/min by adjusting the isoflurane concentration. The body temperature was maintained at 37 °C by a warm waterbed and monitored using a rectal probe. Vital functions were monitored during the whole anesthesia period using SamPC Monitor (version 6.17, Small Animal Instruments Inc.). Anatomical images of the mice were provided by T_2-weighted axial images acquired with a Rapid Acquisition with Relaxation Enhancement sequence (RARE; TR/TE: 2500/30 ms, RARE factor: 6, 10 slices non-contiguous with a gap of 0.08 mm, resolution: 125 × 125 × 800 μm^3). T_2 maps were acquired with the same geometry than the anatomical images using a Multi Slice Multi Echo sequence (MSME; TR/TE: 2500/10 ms; 16 echoes). Quantitative T_2 maps were calculated from the MSME multi-echo trains and assuming mono-exponential decays, using ImageJ (ImageJ version, 1.48 NIH). The volume of interest (VOI) corresponding to the tumor volume were manually delineated on a slice by slice basis on the anatomical images acquired before and after treatment injection, for each animal. These VOIs were applied on corresponding maps to determine the T_2 values. Relative standard deviations (RSD) were calculated as RSD = *SD/mean* T_2, where SD is the standard deviation of the mean T_2 value [28].

2.7. Histological study of tumor tissues

The accumulation of multifunctional nanoparticles in tumor tissue was visualized by histological analysis of tumor tissue after Prussian's blue staining. After MR imaging, the mice were sacrificed and the tumor tissues were surgically removed and fixed in 4% paraformaldehyde and imbedded in paraffin. Representative 5 μm tumor cross-sections were cut and mounted on glass slides. Thereafter the sections were placed in a bath containing 5% potassium hexacyanoferrate (II) trihydrate (Sigma Aldrich) and 5% HCl in distilled water for 30 min at room temperature and protected from light. Tumor sections were counterstained with a 0.1% nuclear fast red aqueous solution (Sigma Aldrich) containing 5% aluminum sulfate for 5 min.

2.8. Statistical analysis

All results arising from *in vivo* antitumor efficacy and *ex vivo* biodistribution are expressed as mean ± SEM. Two-way ANOVA, Bonferroni post-test, Kaplan–Meier survival rate and *t*-test were performed using the software GraphPad Prism 5 for Windows, to demonstrate statistical differences ($p < 0.05$). MRI results were expressed as mean RSD ± SD. One-way ANOVA and Bonferroni post-test were performed using the software GraphPad Prism 5 for Windows, to demonstrate statistical differences ($p < 0.05$).

3. Results

3.1. Physico-chemical characterization

Physico-chemical features of the nanoparticles are summarized in Table 1. Nanoparticles co-loaded with SPIO and PTX presented a similar size of about 240 nm when grafted with RGD or not. They all presented a neutral ζ potential and drug encapsulation efficiency approximately 25%. This corresponds to a paclitaxel-loading of around 1.8 mg/100 mg of polymer. SPIO-loading was about 10 mg/100 mg of polymer. Moreover, they all presented a saturation magnetization around 15 Am^2/kg. In a previous *in vitro* study, we evaluated the drug release from nanoparticles [11]. Briefly, after the initial burst release for about 4 h (50%), the release rate of PTX slowed down and became an almost zero-order rate of release (75% released in 11 days).

3.2. In vivo anti-tumor efficacy

The *in vivo* anti-tumor efficacy of the different targeting strategies was evaluated in CT26-tumor-bearing mice (Fig. 2). All PTX-loaded nanoparticles induced a higher delay in tumor growth than the control group (PBS) (Fig. 2A). Moreover, all the groups treated with active targeting (RGD, MT and RGD + MT) induced a higher delay compared with PT (Fig. 2A). The Kaplan–Meier survival rate was performed (Fig. 2B). PT exhibited a higher survival rate than the untreated group (PBS) with median survival rate of 13 compared to 10 days ($p < 0.01$). No significant difference was observed between RGD and MT with median survival times of 14.7 and 15 days ($p > 0.05$), which are statistically different from the PBS group ($p < 0.01$) and from the PT group ($p < 0.01$). Moreover, one long-term survival mouse was found in the RGD group. Finally, the mice treated with the combination of active and magnetic targeting (RGD + MT) exhibited the highest survival rate with a median survival time of 21.5 days ($p < 0.05$). In this group, there were two long-term survival mice. The benefits of the combination of RGD + MT are illustrated in Fig. 2C. The time to reach a tumor-growing ratio of 13 (endpoint of the PBS group) was prolonged by both RGD and MT treatments compared to the control group (11.7, 12.1, respectively compared to 8.6; $p < 0.001$ and $p < 0.0001$, respectively). The mice treated with RGD-grafted nanoparticles and magnetically targeted nanoparticles (MT) showed an equivalent time to reach a tumor-growing ratio of 13 ($p > 0.05$). The time to reach a tumor-growing ratio of 13 was enhanced when mice were treated with RGD-grafted nanoparticles combined with the magnetic targeting (RGD + MT) when compared to MT or RGD alone (14.8 days *versus* 12.1 and 11.7 days, respectively; $p < 0.01$ and $p < 0.05$).

3.3. Biodistribution using ESR spectroscopy

Biodistribution studies of SPIO/PTX-loaded NPs are illustrated in Fig. 3. Iron accumulations in blood, tumor tissue, liver and lungs were measured using ESR spectroscopy. Blood samples did not show any statistical differences in terms of iron concentration with a mean concentration of around 2 ng/mg of blood for all groups (data not shown). Concerning the iron accumulation in tumor tissues (Fig. 3A), no significant difference was observed between 1 h and 4 h after injection even when using magnetic targeting. The mice treated with RGD showed a 2.5-fold accumulation increase in tumor tissue compared to the group treated with PT with 0.35% of the injected dose and 0.135%, respectively ($p < 0.05$). This accumulation rose to 5-fold in MT (0.737%, $p < 0.001$). The highest iron concentration was

Table 1
Physico-chemical properties of nanoparticles. Size, ζ potential, drug encapsulation efficiency, drug loading, SPIO loading and saturation magnetization (M_{sat}) of SPIO-loaded nanoparticles (SPIO-NP), paclitaxel-loaded nanoparticles (PTX-NP), co-loaded SPIO/paclitaxel nanoparticles (SPIO/PTX-NP) and co-loaded SPIO/paclitaxel nanoparticles grafted with RGD ($n = 5$).

	SPIO-NP	SPIO/PTX-NP	SPIO/PTX-NP RGD
Size (nm)	235.8 ± 8.9	243 ± 9.9	245 ± 1.2
Zeta ζ potential (mV)	−0.16 ± 0.04	−0.02 ± 0.01	−0.42 ± 0.6
Drug encapsulation efficiency (%)	/	24.8 ± 4.9	25.2 ± 2.8
PTX loading (mg/100 mg of polymer)	/	1.84 ± 0.4	1.85 ± 0.2
SPIO-loading (mg/100 mg of polymer)	9.0 ± 1.5	10.4 ± 1.9	10.1 ± 0.6
M_{sat} (Am^2/kg or emu/g)	14.5 ± 0.1	15.1 ± 0.1	14.1 ± 0.1

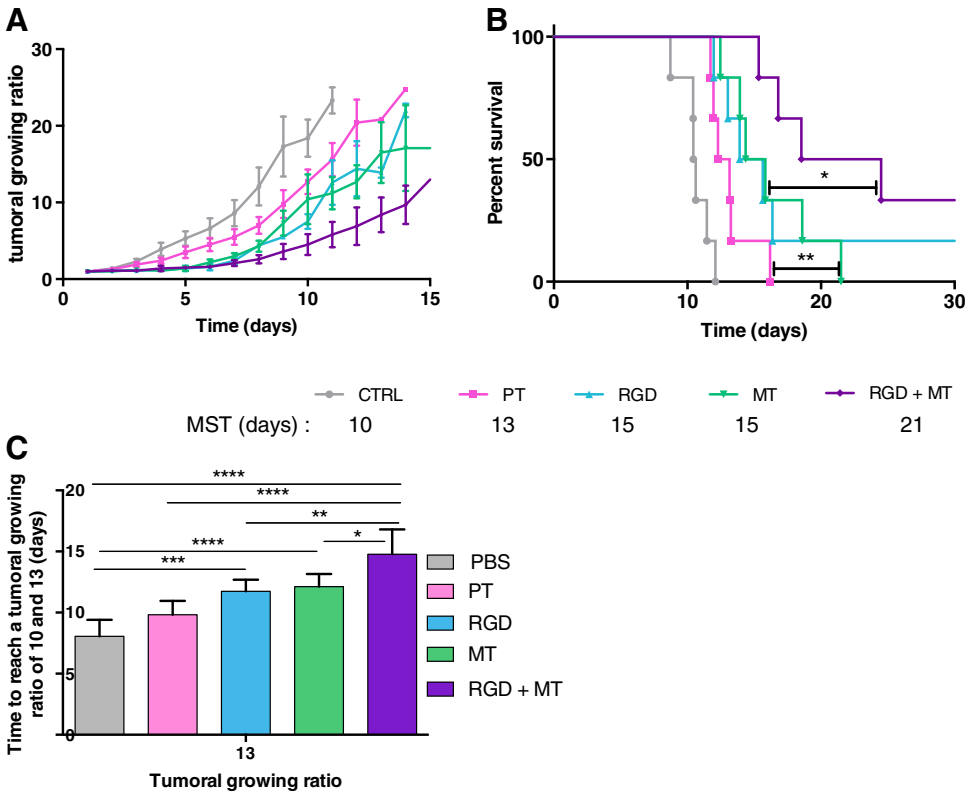

Fig. 2. Tumoral growing ratio and survival rates of CT26-tumor bearing mice. (A) Tumor growth curves of CT26-tumor bearing mice treated with co-loaded SPIO/PTX nanoparticles (PT) (PTX dose = 5 mg/kg), SPIO/PTX-NP grafted with RGD-peptide (RGD), SPIO/PTX-NP followed by 4 h of magnetic targeting (MT) and SPIO/PTX-NP RGD followed by 4 h of magnetic targeting (RGD + MT) or untreated (PBS). The treatment was injected into the tail vein of the mice when tumors reached 27 ± 5 mm ($n = 6$). Results are presented as the average tumor growing ratio ± SEM *versus* time after treatment injection. (B) Survival rates of tumor-bearing mice. Mean survival times (MST) in days were calculated for each group. (C) Comparison of time for tumor to reach a growing ratio of 13 (in days). $^{*}p < 0.05$, $^{**}p < 0.01$, $^{***}p < 0.001$, $^{****}p < 0.0001$.

obtained in the mice treated with the combination of RGD + MT with an 8-fold increase in iron accumulation (1.12% of the injected dose). The iron uptake by the liver (Fig. 3B) was dominant for all treatment groups with iron concentration rising up to 35% of the injected dose. However, after 4 h of MT, this iron uptake was drastically reduced to 11.29% of the injected dose ($p < 0.001$). Interestingly, the RGD-, MT- and RGD + MT-treated groups showed a highly significant decrease of the iron accumulation in lungs compared to control and PT-treated groups with 0.52%, 0.43% and 0.47% of the injected dose for the RGD-, MT- and RGD + MT-treated groups, respectively compared to 1.31% and 1.21% of the injected dose for control and PT-treated group after 1 h ($p < 0.001$, Fig. 3C).

3.4. Histological analysis

Fig. 4 shows representative histological sections of tumor tissues stained with Prussian blue to label the SPIO nanoparticles. Blue spots indicating the presence of SPIO are pointed out by white arrows. As seen in Fig. 4A, no blue coloration was observed in untreated tumor tissue. Only a few blue spots were observed in tumor treated with PT (Fig. 4B). There were more blue spots in tissues of mice treated by RGD (Fig. 4C). These blue spots were even more numerous in tumor tissue when using MT (Fig. 4D). Nevertheless, the most colored sections were obtained for the mice of the RGD + MT group (Fig. 4E).

3.5. In vivo MRI

To detect the contrast enhancement provided by the injection of the different treatments, MR imaging of mice were performed before and 4 h after injection. T_2-weighted images, obtained with different TEs from the MSME sequence, showed very low signal intensity in the areas characterized by the presence of SPIO (Fig. 5, red arrows). For this reason, the T_2 value corresponding to these areas could not be determined. To estimate the local disturbance induced by SPIO in MRI, RSD of T_2 is commonly used [28]. Injection of the passive targeted nanoparticles (PT) induced no visible darkening of the tumor region (Fig. 5A). No significant change in RSD was observed ($p > 0.05$) (Fig. 6). The mice treated with actively targeted nanoparticles (RGD) showed a slight darkening of the tumor region with a few darker spots located into the tumor tissue pointed out by arrow-head (Fig. 5B). This effect was reflected by a tendency of a 3-times increase in RSD after injection ($p > 0.05$) (Fig. 6). As for the mice treated with magnetic targeted treatment (MT), many dark spots were clearly found in the tumor region (Fig. 5C) inducing a 30-fold increase in RSD after injection ($p < 0.001$) (Fig. 6). The combination of magnetic targeting and active targeting induced also a high darkening contrast (Fig. 5D) translated into a 40-fold increase in RSD after injection ($p < 0.001$) (Fig. 6). The difference between MT and RGD + MT was not significant ($p > 0.05$) but a tendency of a larger increase in RSD was observed for RGD + MT (3.4 ± 0.42 vs 4.4 ± 0.67, for MT and RGD + MT, respectively).

4. Discussion

A major challenge to address in cancer therapy lies in improving the amount of drug reaching the tumor to have an efficient treatment while limiting the damages to healthy tissues. Therefore, different targeting strategies have been developed [7,29]. In this study, we compared four targeting strategies of multifunctional nanoparticles loaded with an anti-cancer drug and a imaging agent in terms of anti-tumor efficacy, biodistribution and magnetic resonance imaging capabilities: passive targeting (PT), active $\alpha_v\beta_3$ targeting (RGD), magnetic targeting (MT)

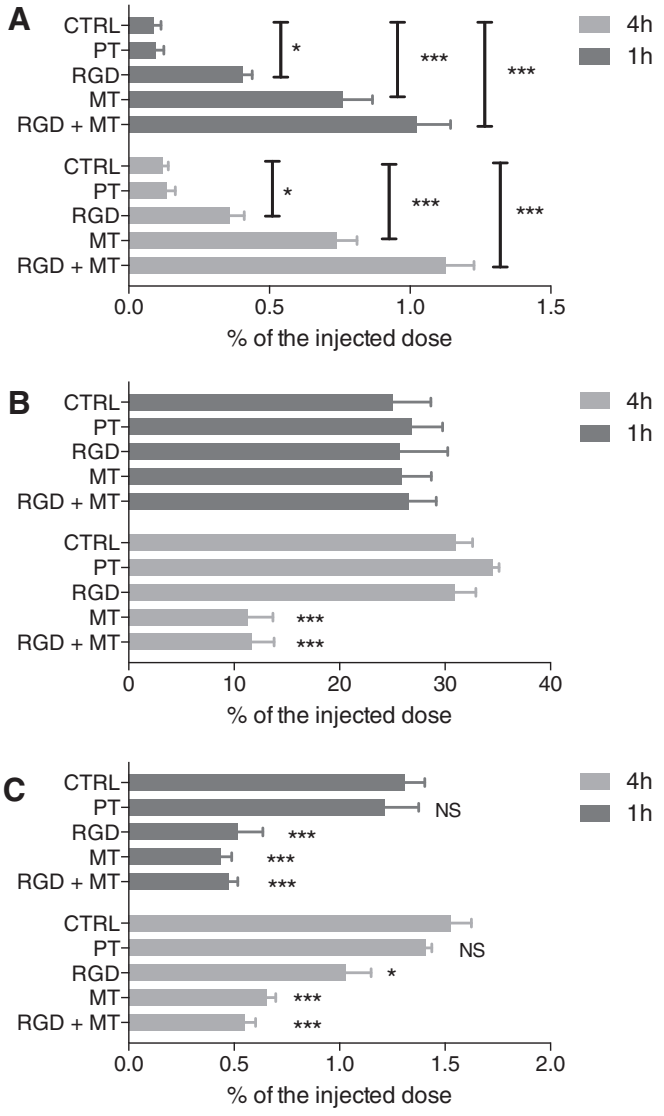

Fig. 3. Biodistribution of multifunctional nanoparticles. Biodistribution of multifunctional nanoparticles using ESR spectroscopy, 1 or 4 h after injection of the treatment. 5 groups were defined: SPIO-loaded nanoparticles (CTRL), PT, RGD, MT and RGD + MT. (A) Iron accumulation in tumor tissue in ng/mg of tissue ($n = 5$). (B) Iron accumulation in liver ($n = 5$). (C) Iron accumulation in lungs ($n = 5$). *$p < 0.05$, ***$p < 0.001$, NS: not significant.

and the combination of the two latest (RGD + MT). The current multifunctional nanoparticles incorporated SPIO for their diagnostic and superparamagnetic properties and PTX for its therapeutic properties.

All experiments (PTX anti-cancer efficacy, biodistribution, MRI and histological studies) were consistent with each other indicating that active targeting (RGD) was more effective than passive targeting (PT). Magnetic targeting (MT) showed a better efficacy compared to active targeting (RGD) in biodistribution, MRI and histological studies. PTX anti-cancer efficacy, biodistribution and histological studies confirmed that the most effective targeting was obtained using a double targeting (RGD + MT).

Magnetic resonance imaging (MRI) is a clinical widely used non-invasive imaging technique, presenting a high spatial resolution, which is suitable for cancer detection and therapeutic response assessment [12,30]. However, its major limitation consists of a relatively low sensitivity. Superparamagnetic iron oxides (SPIO) as MRI contrast agent address this limitation. SPIO can produce predominant T_2 relaxation effect, resulting in a signal reduction on T_2-weighted images. The magnetic field heterogeneity around the particles, through which water molecules diffuse, induces the dephasing of the proton magnetic moments. Consequently, a T_2 effective transverse relaxation is shortened. Moreover, with their high magnetic properties, SPIO are among the most suitable candidates to achieve magnetic targeting abilities by using an external magnet [31]. However, when SPIO concentration is very high, a fitting deficiency can occur and lead to difficulties in measuring T_2 values. Indeed, high concentration of SPIO in the tumor produced a too fast decrease of the T_2 value resulting in a non-exponential relationship. Thus, it was impossible to measure a proper T_2 value at these sites. Therefore, we measured a relative standard deviation of these T_2 values in the ROI. RSD is a measure of tumor heterogeneity after the SPIO injection. This method is commonly used in MRI when the T_2 signal is too heterogeneous [28].

Recently, numerous publications have reported various polymer-based nanocarriers (PLGA, PLLA, HPMA, PCL, *etc.*) for magnetic-imaging [32–35]. These SPIO-loaded nanocarriers are generally limited because of (i) their lack of functional groups on their surface for covalent modification, (ii) their low capacity for drug loading and (iii) the fact that the use of most polymers is not approved by the FDA/EMA, limiting their potential translation to the clinic [21]. So far, many researchers have shown interest in active targeting [11,36,37] and in magnetic targeting [16,26]. However, only few have shown *in vivo* efficacy in both therapeutic and imaging approaches.

An in vivo anti-tumor efficacy study showed a significant longer regrowth delay with a longer survival time for mice treated with actively-targeted nanoparticles (RGD) compared to the passively-targeted nanoparticles. This result is consistent with our previous study [11]. The potential advantage of targeted delivery may result from an altered intracellular distribution. Both targeted and non-targeted systems arrive at the tumor site *via* the EPR effect, after which the mechanism of tumor cell internalization is enhanced by the presence of surface ligands *via* a receptor-mediated endocytosis [38,39]. On the contrary, non-targeted nanoparticles mainly enter into the cells *via* pinocytosis [40–42]. Furthermore, this better anti-tumor efficacy can be easily explained by the increased accumulation in tumor tissue. Indeed, *ex-vivo* biodistribution, histological studies and MRI confirmed the iron concentration increase in tumor tissue suggesting a better accumulation of nanoparticles. However, despite this better accumulation in tumor tissue, a major issue that remains to be solved is the massive uptake by the liver. This phenomenon is well known and described in the literature [43]. Zhang et al. reported an accumulation of RGD-grafted magnetite PLGA-based nanoclusters of 35% of the injected dose in the liver [37]. For this reason, SPIO-loaded nanoparticles are usually used as contrast agent for liver imaging [34]. This particular point raises the question of the toxicity of such accumulation. Analysis of the literature shows conflicting results on the toxicity of SPIO. Some studies have shown that SPIO could generate a production of ROS in liver cells that could lead to toxicity [44]. However, this toxicity seems to depend on the particle shape, size, charge and dose [45]. Moreover, in normal circumstances, the injected iron is expected to be sequestered by Kupffer cells, metabolized and regulated by normal physiological iron homeostatic mechanisms [46]. This SPIO sequestration seems to protect liver cells from apoptosis since only free iron oxides proved to be toxic. Indeed, Jain et al. showed that the intra-venous administration of oleic acid coated SPIO (10 mg Fe/kg) did not result in any notable alteration of the liver functionality [47]. Nevertheless, repeated dosing of SPIO in short intervals would not be a desirable option in imaging and drug delivery since it could lead to a surpassed transferrin iron-binding capacity and, therefore, to high free iron concentration [46,48]. Hence, in the view of a translational approach, further toxicity assessment should be performed.

Magnetic targeting showed a better nanoparticle accumulation in tumor compared to active targeting in *ex-vivo* biodistribution, histological study and MRI. As expected, this better accumulation was correlated with a longer survival time and a longer regrowth delay compared to the passively-targeted group. Lübbe et al. were the pioneers in using an external magnetic field to guide a treatment [49]. Later, numerous

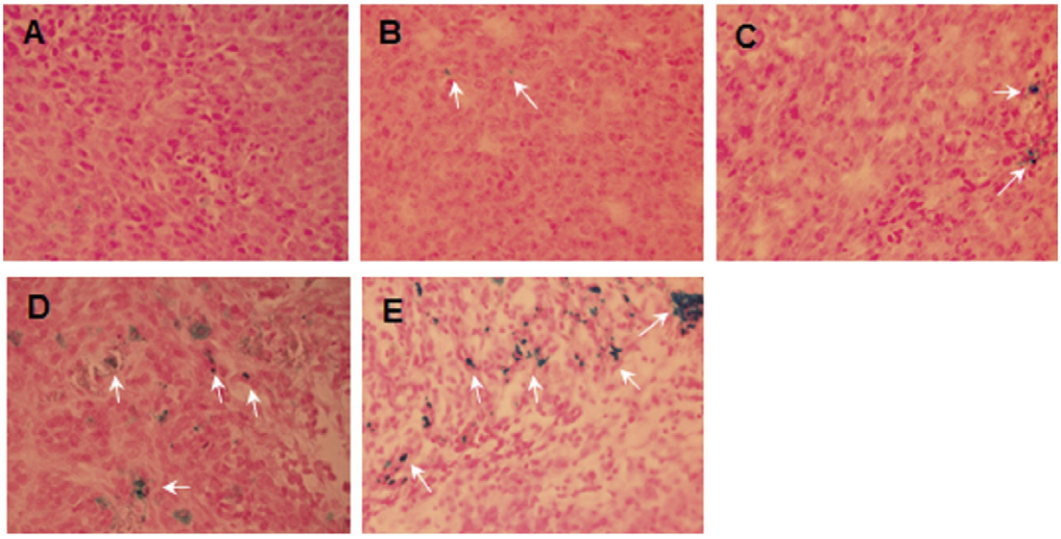

Fig. 4. Histological study of tumor tissue using Prussian blue staining. A: CTRL, B: SPIO/PTX-NP treated mouse, C: SPIO/PTX-NP RGD treated mouse, D: SPIO/PTX-NP treated group with magnetic targeting. E: SPIO/PTX-NP RGD treated group with magnetic targeting.

studies used this method with magnetic field strength ranging from 0.4 to 4 T [16,50–52]. The success of magnetic targeting is limited by inadequate magnetic gradients, thus, by the distance between the magnets and the target site. The magnetic targeting would be more effective in regions closer to the magnets. In this experiment, a 1.1 T neodyme permanent magnet was used to create an external magnetic field to accumulate the treatment in the tumor. For superficial tumors, this strategy can be easily done by placing the permanent magnet outside of the body at the surface of the tumor [16,50,53]. Since the magnetism is size-dependent, particles size can also influence the attraction by the magnet. Indeed, small particles are less susceptible to be attracted than large particles [46]. Finally, magnetic targeting efficacy is also dependent on the saturation magnetization, which refers to the maximum magnetization possible. Generally, nanoparticles with higher saturation magnetization are preferred because they provide higher sensitivity and efficiency [54]. Our particles showed a relatively low saturation magnetization (Ms) compared to the free SPIO described in the literature [55,56]. Indeed, while the use of a polymer coating around SPIO has been shown to increase relaxivities (R_2) or reduce transverse relaxation times (T_2) making, thus, a more effective contrast agent, at the same time, it is associated with a change in the anisotropy constant leading to a further reduction in magnetization [57]. This phenomenon constitutes another limitation to magnetic targeting. Further investigations should be performed on the modulation of nanoparticle physical parameters (size, shape, composition, and shell-core architecture) to optimize the properties of these magnetic nanoparticles for improved magnetic targeting applications.

The most impressive results were undoubtedly obtained with the combination of both active and magnetic strategies. Indeed, the double targeting-treated group of mice showed the most important regrowth delay compared to all the other groups. Moreover, two mice were long-time survivor in the RGD + MT-treated group. This better efficacy of combined RGD + MT targeting could be explained by a double phenomenon: (i) Both targeted and non-targeted systems arrive at the tumor *via* the EPR effect. Magnetic targeting promotes the accumulation of nanoparticles near the magnet and, thus, near the tumor cells. However, to date, studies showed that this strategy did not promote nanoparticle entrance into the cells [44,58]. Mechanisms of tumor internalization for both non-targeted and magnetically-targeted nanoparticles mostly involve macropinocytosis [58,59]. On the other hand, RGD-targeted nanoparticles are internalized by both tumor cells and endothelial cells (which are expressing $\alpha_v\beta_3$integrin) *via* receptor-mediated endocytosis, as abovementioned. Consequently, nanoparticle intratumoral distribution could shift from the extracellular compartment to the tumor cell intracellular compartment [38]. Therefore, combining active targeting (RGD) and magnetic targeting (MT) could enhance anti-tumor efficacy by both an enhanced accumulation (by MT) and an enhanced entrance (*via* $\alpha_v\beta_3$receptor-mediated endocytosis — by RGD targeting).

(ii) For non-grafted nanoparticles only the EPR effect can explain the accumulation of drug-loaded nanocarriers into the tumor. By contrast, RGD-targeted nanoparticles exert a double active targeting of both endothelial and cancer cells. Indeed, $\alpha_v\beta_3$integrin is expressed on endothelial cells of neoangiogenic vessels, allowing the binding of circulating RGD-nanoparticles resulting in subsequently tumor cells death by lack of oxygen and nutrients, and on tumor cells [7,60,61]. This anti-angiogenic effect of the active targeting of drug-loaded RGD-nanoparticles constitute an advantage to the RGD-nanoparticles treatment since this effect does not rely on the penetration of nanoparticles into the tumor interstitium which is complicated by the high interstitial fluid pressure [62,63].

The remaining question is why did not all the mice respond the same way? Since angiogenesis is regulated by numerous factors including tumor size, environmental factors, expression level of multiple anti- and pro-angiogenic factors, its level is expected to be different in each subject (inter-individual variability) [64,65].

Unsurprisingly, this better anti-cancer efficacy was correlated with a higher nanoparticle accumulation in the tumor (shown by both ESR spectroscopy and histological studies). The lack of difference in the T_2 RSD of MT and RGD + MT could be due to the very fast decrease in the T_2 value obtained in both groups leading to the fitting deficiency as aforementioned. Moreover, MRI is less sensitive compared to ESR spectroscopy [66] Furthermore, using such a combination could be useful to potentialize the effect of active targeting. Indeed, since active targeting is a saturable process [67] and sometimes lacks selectivity, it becomes more and more interesting to combine several targeting strategies [68].

These results confirmed our hypothesis. Indeed, there was a rationale to think that two targeting strategies would show better results compared to a single strategy. Many groups have studied a double targeting strategy for delivery purposes. Recently, Fang et al. used a combination of MT and lactoferrin [69]. Yang et al. have studied a double RGD and NGR targeting [70]. However, to our knowledge, this is the first study having investigated the combination of both $\alpha_v\beta_3$integrin-targeting and magnetic targeting for a theranostic purpose. RGD targeting is a very promising strategy since it can target

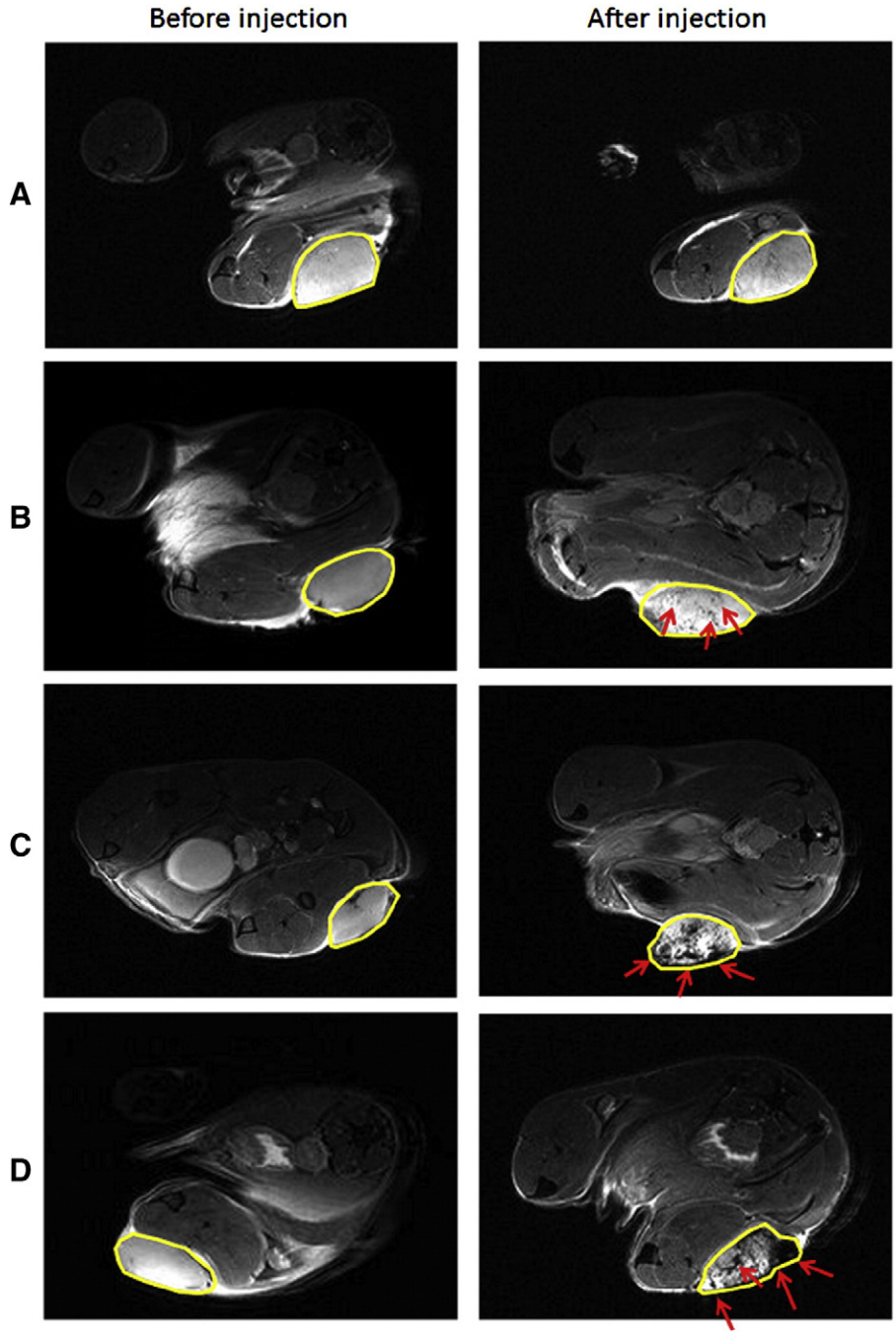

Fig. 5. MRI imaging. T2-weighted images, obtained from MSME sequence (TE = 10 ms) of CT26-tumor bearing mice pre-injection and 4 h after injection. The position of the dark region in tumor is indicated by red arrows (n = 5). A: PT, B: RGD, C: MT, D: RGD + MT.

both neoangiogenic endothelial cells and tumors cells. Moreover, $\alpha_v\beta_3$ plays an important role in angiogenesis [71]. Finally, in our previous study, we demonstrated the efficacy of targeting to tumor endothelium of RGD-grafted nanoparticles and their better anti-tumor efficacy [8].

Solid tumors are known to be highly heterogeneous either depending on the cancer type, patient or even on the disease stage (inter-tumor heterogeneity). Moreover, different cell types can be found inside a solid tumor (intra-tumor heterogeneity). Furthermore, in response to any given therapy, solid tumors inevitably evolve, leading to strong difficulties in managing cancer therapy. Therefore, there is a critical need in developing personalized therapy [72,73]. The combination of imaging and therapeutic capabilities in the same vector could provide a useful tool in addressing this challenge. Indeed, such theranostic platforms allow the molecular diagnosis by imaging to verify the expression of cancer biomarker to guide target-specific therapy. Furthermore, it enables to assess the efficacy of the treatment at different stages of the therapy then using those results to intelligently modify the strategy for cancer treatment (real-time monitoring) [1,72]. The multifunctional $\alpha_v\beta_3$-targeted nanoparticles developed in this study showed promising results in terms of anti-tumor efficiency and imaging abilities when combined with magnetic targeting. Finally, their imaging abilities could be useful to monitor the biodistribution of these multifunctional nanoparticles after injection to the patient in a first step. Thereafter, on the basis of this non-invasive imaging insight into the target site, and possibly undesirable liver accumulation it would be possible to evaluate a benefit/risk ratio and, if favorable, select the patient for the

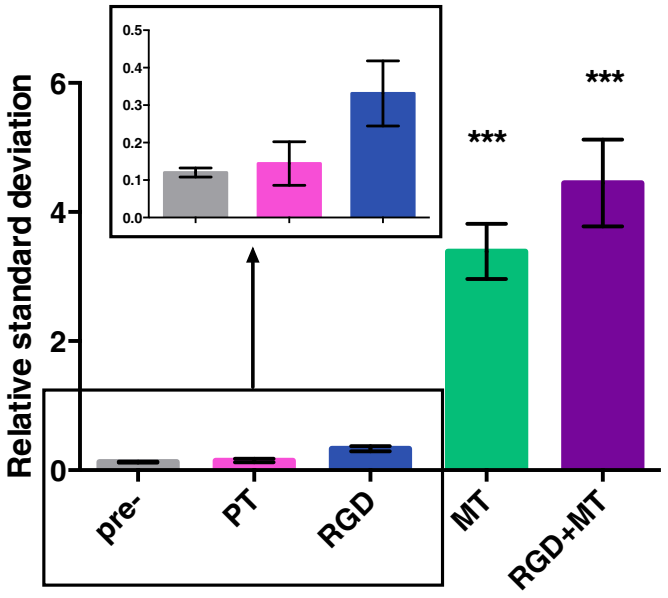

Fig. 6. MRI quantification. Mean RSD (Relative Standard Deviation) calculation of the tumor region pre- and 4 h after injection of PT, RGD, MT and RGD + MT (results expressed as mean ± SD, n = 5). ***$p < 0.001$.

treatment. This particular application could be of great interest to limit the treatment of non-responding patients and patients at high risk of undesirable toxicity.

This study also proves that MRI could be predictive of the anti-cancer treatment efficacy. This finding could be interesting from the perspective of a translational approach in the management of therapeutic treatment and personalized therapy, using these multifunctional nanoparticles as theranostics.

5. Conclusion

This study is the first to compare *in vivo* four targeting strategies for multifunctional nanoparticles in terms of anti-cancer efficacy, *ex-vivo* biodistribution, and MRI contrast agent efficiency. The most effective targeting strategy for imaging and therapeutic purposes was obtained by the use of a combination of active strategy using RGD-grafted nanoparticles and magnetic targeting.

Acknowledgments

This work was supported by the FSR (Université Catholique de Louvain) and the National Fund of Scientific Research (FNRS, Belgium). Fabienne Danhier is a post-doctoral researcher of the FNRS.

References

[1] T. Lammers, F. Kiessling, W.E. Hennink, G. Storm, Nanotheranostics and image-guided drug delivery: current concepts and future directions, Mol. Pharm. 7 (6) (2010) 1899–1912.
[2] N. Ahmed, H. Fessi, A. Elaissari, Theranostic applications of nanoparticles in cancer, Drug Discov. Today 17 (17–18) (2012) 928–934.
[3] J. Xie, S. Lee, X. Chen, Nanoparticle-based theranostic agents, Adv. Drug Deliv. Rev. 62 (11) (2010) 1064–1079.
[4] S.M. Janib, A.S. Moses, J.A. MacKay, Imaging and drug delivery using theranostic nanoparticles, Adv. Drug Deliv. Rev. 62 (11) (2010) 1052–1063.
[5] L.Y. Rizzo, B. Theek, G. Storm, F. Kiessling, T. Lammers, Recent progress in nanomedicine: therapeutic, diagnostic and theranostic applications, Curr. Opin. Biotechnol. 24 (6) (2013) 1159–1166.
[6] T. Lammers, L.Y. Rizzo, G. Storm, F. Kiessling, Personalized nanomedicine, Clin. Cancer Res. 18 (18) (2012) 4889–4894.
[7] F. Danhier, O. Feron, V. Préat, To exploit the tumor microenvironment: passive and active tumor targeting of nanocarriers for anti-cancer drug delivery, J. Control. Release 148 (2) (2010) 135–146.
[8] F. Danhier, A. Le Breton, V. Préat, RGD-based strategies to target alpha(v) beta(3) integrin in cancer therapy and diagnosis, Mol. Pharm. 9 (11) (2012) 2961–2973.
[9] H. Maeda, J. Wu, T. Sawa, Y. Matsumura, K. Hori, Tumor vascular permeability and the EPR effect in macromolecular therapeutics: a review, J. Control. Release 65 (1–2) (2000) 271–284.
[10] S. Taurin, H. Nehoff, K. Greish, Anticancer nanomedicine and tumor vascular permeability; where is the missing link? J. Control. Release 164 (3) (2012) 265–275.
[11] F. Danhier, B. Vroman, N. Lecouturier, N. Crokart, V. Pourcelle, H. Freichels, C. Jérôme, J. Marchand-Brynaert, O. Feron, V. Préat, Targeting of tumor endothelium by RGD-grafted PLGA-nanoparticles loaded with paclitaxel, J. Control. Release 140 (2) (2009) 166–173.
[12] Y. Liu, Y. Yang, C. Zhang, A concise review of magnetic resonance molecular imaging of tumor angiogenesis by targeting integrin alphavbeta3 with magnetic probes, Int. J. Nanomedicine 8 (2013) 1083–1093.
[13] E. Garanger, D. Boturyn, J.L. Coll, M.C. Favrot, P. Dumy, Multivalent RGD synthetic peptides as potent alphaVbeta3 integrin ligands, Org. Biomol. Chem. 4 (10) (2006) 1958–1965.
[14] E.A. Murphy, B.K. Majeti, L.A. Barnes, M. Makale, S.M. Weis, K. Lutu-Fuga, W. Wrasidlo, D.A. Cheresh, Nanoparticle-mediated drug delivery to tumor vasculature suppresses metastasis, Proc. Natl. Acad. Sci. U. S. A. 105 (27) (2008) 9343–9348.
[15] H.N. Son, J.O. Nam, S. Kim, I.S. Kim, Multiple FAS1 domains and the RGD motif of TGFBI act cooperatively to bind alphavbeta3 integrin, leading to anti-angiogenic and anti-tumor effects, Biochim. Biophys. Acta 1833 (10) (2013) 2378–2388.
[16] J.L. Arias, L.H. Reddy, M. Othman, B. Gillet, D. Desmaele, F. Zouhiri, F. Dosio, R. Gref, P. Couvreur, Squalene based nanocomposites: a new platform for the design of multifunctional pharmaceutical theragnostics, ACS Nano 5 (2) (2011) 1513–1521.
[17] A.J. Cole, V.C. Yang, A.E. David, Cancer theranostics: the rise of targeted magnetic nanoparticles, Trends Biotechnol. 29 (7) (2011) 323–332.
[18] F. Danhier, P. Danhier, N. Magotteaux, G. De Preter, B. Ucakar, O. Karroum, B. Jordan, B. Gallez, V. Préat, Electron paramagnetic resonance highlights that the oxygen effect contributes to the radiosensitizing effect of paclitaxel, PLoS One 7 (7) (2012) e40772.
[19] K.A. Radermacher, N. Beghein, S. Boutry, S. Laurent, E.L. Vander, R.N. Muller, B.F. Jordan, B. Gallez, *In vivo* detection of inflammation using pegylated iron oxide particles targeted at E-selectin: a multimodal approach using MR imaging and EPR spectroscopy, Invest. Radiol. 44 (7) (2009) 398–404.
[20] K.A. Radermacher, J. Magat, C. Bouzin, S. Laurent, T. Dresselaers, U. Himmelreich, S. Boutry, I. Mahieu, E.L. Vander, O. Feron, R.N. Muller, B.F. Jordan, B. Gallez, Multimodal assessment of early tumor response to chemotherapy: comparison between diffusion-weighted MRI, 1H-MR spectroscopy of choline and USPIO particles targeted at cell death, NMR Biomed. 25 (4) (2012) 514–522.
[21] N. Schleich, P. Sibret, P. Danhier, B. Ucakar, S. Laurent, R.N. Muller, C. Jérôme, B. Gallez, V. Préat, F. Danhier, Dual anticancer drug/superparamagnetic iron oxide-loaded PLGA-based nanoparticles for cancer therapy and magnetic resonance imaging, Int. J. Pharm. 447 (1–2) (2013) 94–101.
[22] M. Garinot, V. Fievez, V. Pourcelle, F. Stoffelbach, A. des Rieux, L. Plapied, I. Theate, H. Freichels, C. Jérôme, J. Marchand-Brynaert, Y.J. Schneider, V. Préat, PEGylated PLGA-based nanoparticles targeting M cells for oral vaccination, J. Control. Release 120 (3) (2007) 195–204.
[23] V. Pourcelle, H. Freichels, F. Stoffelbach, R. Auzely-Velty, C. Jérôme, J. Marchand-Brynaert, Light induced functionalization of PCL-PEG block copolymers for the covalent immobilization of biomolecules, Biomacromolecules 10 (4) (2009) 966–974.
[24] P. Danhier, G. De Preter, S. Boutry, I. Mahieu, P. Leveque, J. Magat, V. Haufroid, P. Sonveaux, C. Bouzin, O. Feron, R.N. Muller, B.F. Jordan, B. Gallez, Electron paramagnetic resonance as a sensitive tool to assess the iron oxide content in cells for MRI cell labeling studies, Contrast Media Mol. Imaging 7 (3) (2012) 302–307.
[25] F. Danhier, N. Lecouturier, B. Vroman, C. Jérôme, J. Marchand-Brynaert, O. Feron, V. Préat, Paclitaxel-loaded PEGylated PLGA-based nanoparticles: *in vitro* and *in vivo* evaluation, J. Control. Release 133 (1) (2009) 11–17.
[26] H.W. Yang, M.Y. Hua, H.L. Liu, R.Y. Tsai, S.T. Pang, P.H. Hsu, H.J. Tang, T.C. Yen, C.K. Chuang, An epirubicin-conjugated nanocarrier with MRI function to overcome lethal multidrug-resistant bladder cancer, Biomaterials 33 (15) (2012) 3919–3930.
[27] J.A. Lyons, B.J. Sheahan, S.E. Galbraith, R. Mehra, G.J. Atkins, M.N. Fleeton, Inhibition of angiogenesis by a Semliki Forest virus vector expressing VEGFR-2 reduces tumour growth and metastasis in mice, Gene Ther. 14 (6) (2007) 503–513.
[28] J.M. Oakes, E.C. Breen, M. Scadeng, G.S. Tchantchou, C. Darquenne, MRI-based measurements of aerosol deposition in the lung of healthy and elastase-treated rats, J. Appl. Physiol. (1985) 116 (12) (2014) 1561–1568.
[29] I.K. Kwon, S.C. Lee, B. Han, K. Park, Analysis on the current status of targeted drug delivery to tumors, J. Control. Release 164 (2) (2012) 108–114.
[30] K. Brindle, New approaches for imaging tumour responses to treatment, Nat. Rev. Cancer 8 (2) (2008) 94–107.
[31] S. Laurent, M. Mahmoudi, Superparamagnetic iron oxide nanoparticles: promises for diagnosis and treatment of cancer, Int. J. Mol. Epidemiol. Genet. 2 (4) (2011) 367–390.
[32] M. Hamoudeh, F.A. Al, E. Canet-Soulas, F. Bessueille, D. Leonard, H. Fessi, Elaboration of PLLA-based superparamagnetic nanoparticles: characterization, magnetic behaviour study and *in vitro* relaxivity evaluation, Int. J. Pharm. 338 (1–2) (2007) 248–257.
[33] Y. Ling, K. Wei, Y. Luo, X. Gao, S. Zhong, Dual docetaxel/superparamagnetic iron oxide loaded nanoparticles for both targeting magnetic resonance imaging and cancer therapy, Biomaterials 32 (29) (2011) 7139–7150.

[34] J. Lu, S. Ma, J. Sun, C. Xia, C. Liu, Z. Wang, X. Zhao, F. Gao, Q. Gong, B. Song, X. Shuai, H. Ai, Z. Gu, Manganese ferrite nanoparticle micellar nanocomposites as MRI contrast agent for liver imaging, Biomaterials 30 (15) (2009) 2919–2928.
[35] M. Talelli, C.J. Rijcken, T. Lammers, P.R. Seevinck, G. Storm, C.F. van Nostrum, W.E. Hennink, Superparamagnetic iron oxide nanoparticles encapsulated in biodegradable thermosensitive polymeric micelles: toward a targeted nanomedicine suitable for image-guided drug delivery, Langmuir 25 (4) (2009) 2060–2067.
[36] R.Y. Lin, K. Dayananda, T.J. Chen, C.Y. Chen, G.C. Liu, K.L. Lin, Y.M. Wang, Targeted RGD nanoparticles for highly sensitive *in vivo* integrin receptor imaging, Contrast Media Mol. Imaging 7 (1) (2012) 7–18.
[37] F. Zhang, X. Huang, L. Zhu, N. Guo, G. Niu, M. Swierczewska, S. Lee, H. Xu, A.Y. Wang, K.A. Mohamedali, M.G. Rosenblum, G. Lu, X. Chen, Noninvasive monitoring of orthotopic glioblastoma therapy response using RGD-conjugated iron oxide nanoparticles, Biomaterials 33 (21) (2012) 5414–5422.
[38] A. Prokop, J.M. Davidson, Nanovehicular intracellular delivery systems, J. Pharm. Sci. 97 (9) (2008) 3518–3590.
[39] M. Wang, M. Thanou, Targeting nanoparticles to cancer, Pharmacol. Res. 62 (2) (2010) 90–99.
[40] M.P. Melancon, R.J. Stafford, C. Li, Challenges to effective cancer nanotheranostics, J. Control. Release 164 (2) (2012) 177–182.
[41] R.A. Petros, J.M. DeSimone, Strategies in the design of nanoparticles for therapeutic applications, Nat. Rev. Drug Discov. 9 (8) (2010) 615–627.
[42] P.E. Stromhaug, T.O. Berg, T. Gjoen, P.O. Seglen, Differences between fluid-phase endocytosis (pinocytosis) and receptor-mediated endocytosis in isolated rat hepatocytes, Eur. J. Cell Biol. 73 (1) (1997) 28–39.
[43] N. Bertrand, J.C. Leroux, The journey of a drug-carrier in the body: an anatomo-physiological perspective, J. Control. Release 161 (2) (2012) 152–163.
[44] J.E. Bae, M.I. Huh, B.K. Ryu, J.Y. Do, S.U. Jin, M.J. Moon, J.C. Jung, Y. Chang, E. Kim, S.G. Chi, G.H. Lee, K.S. Chae, The effect of static magnetic fields on the aggregation and cytotoxicity of magnetic nanoparticles, Biomaterials 32 (35) (2011) 9401–9414.
[45] W.J. Yang, J.H. Lee, S.C. Hong, J. Lee, J. Lee, D.-W. Han, Difference between Toxicities of Iron Oxide Magnetic Nanoparticles with Various Surface-Functional Groups against Human Normal Fibroblasts and Fibrosarcoma Cells, Materials 6 (2013) 4689–4706.
[46] S. Laurent, A.A. Saei, S. Behzadi, A. Panahifar, M. Mahmoudi, Superparamagnetic iron oxide nanoparticles for delivery of therapeutic agents: opportunities and challenges, Expert Opin. Drug Deliv. (2014) 1–22.
[47] T.K. Jain, M.K. Reddy, M.A. Morales, D.L. Leslie-Pelecky, V. Labhasetwar, Biodistribution, clearance, and biocompatibility of iron oxide magnetic nanoparticles in rats, Mol. Pharm. 5 (2) (2008) 316–327.
[48] L.H. Reddy, J.L. Arias, J. Nicolas, P. Couvreur, Magnetic nanoparticles: design and characterization, toxicity and biocompatibility, pharmaceutical and biomedical applications, Chem. Rev. 112 (11) (2012) 5818–5878.
[49] A.S. Lubbe, C. Bergemann, W. Huhnt, T. Fricke, H. Riess, J.W. Brock, D. Huhn, Preclinical experiences with magnetic drug targeting: tolerance and efficacy, Cancer Res. 56 (20) (1996) 4694–4701.
[50] C. Alexiou, W. Arnold, R.J. Klein, F.G. Parak, P. Hulin, C. Bergemann, W. Erhardt, S. Wagenpfeil, A.S. Lubbe, Locoregional cancer treatment with magnetic drug targeting, Cancer Res. 60 (23) (2000) 6641–6648.
[51] B. Chertok, B.A. Moffat, A.E. David, F. Yu, C. Bergemann, B.D. Ross, V.C. Yang, Iron oxide nanoparticles as a drug delivery vehicle for MRI monitored magnetic targeting of brain tumors, Biomaterials 29 (4) (2008) 487–496.
[52] D.H. Kim, K.N. Kim, K.M. Kim, Y.K. Lee, Targeting to carcinoma cells with chitosan- and starch-coated magnetic nanoparticles for magnetic hyperthermia, J. Biomed. Mater. Res. A 88 (1) (2009) 1–11.
[53] A.S. Lubbe, C. Bergemann, H. Riess, F. Schriever, P. Reichardt, K. Possinger, M. Matthias, B. Dorken, F. Herrmann, R. Gurtler, P. Hohenberger, N. Haas, R. Sohr, B. Sander, A.J. Lemke, D. Ohlendorf, W. Huhnt, D. Huhn, Clinical experiences with magnetic drug targeting: a phase I study with 4′-epidoxorubicin in 14 patients with advanced solid tumors, Cancer Res. 56 (20) (1996) 4686–4693.
[54] M. Colombo, S. Carregal-Romero, M.F. Casula, L. Gutierrez, M.P. Morales, I.B. Bohm, J.T. Heverhagen, D. Prosperi, W.J. Parak, Biological applications of magnetic nanoparticles, Chem. Soc. Rev. 41 (11) (2012) 4306–4334.
[55] S. Larumbe, C. Gomez-Polo, J.I. Perez-Landazabal, J.M. Pastor, Effect of a SiO2 coating on the magnetic properties of Fe3O4 nanoparticles, J. Phys. Condens. Matter 24 (26) (2012) 266007.
[56] N. Shamim, L. Hong, K. Hidajat, M.S. Uddin, Thermosensitive polymer (N-isopropylacrylamide) coated nanomagnetic particles: preparation and characterization, Colloids Surf. B: Biointerfaces 55 (1) (2007) 51–58.
[57] A.G. Kolhatkar, A.C. Jamison, D. Litvinov, R.C. Willson, T.R. Lee, Tuning the magnetic properties of nanoparticles, Int. J. Mol. Sci. 14 (8) (2013) 15977–16009.
[58] P. Kocbek, S. Kralj, M.E. Kreft, J. Kristl, Targeting intracellular compartments by magnetic polymeric nanoparticles, Eur. J. Pharm. Sci. 50 (1) (2013) 130–138.
[59] A. Kumari, S.K. Yadav, Cellular interactions of therapeutically delivered nanoparticles, Expert Opin. Drug Deliv. 8 (2) (2011) 141–151.
[60] J. Folkman, Tumor angiogenesis: therapeutic implications, N. Engl. J. Med. 285 (1971) 1182–1186.
[61] R.K. Jain, D.G. Duda, J.W. Clark, J.S. Loeffler, Lessons from phase III clinical trials on anti-VEGF therapy for cancer, Nat. Clin. Pract. Oncol 3 (2006) 24–40.
[62] C. Bouzin, O. Feron, Targeting tumor stroma and exploiting mature tumor vasculature to improve anti-cancer drug delivery, Drug Resist. Updat. 10 (3) (2007) 109–120.
[63] R.K. Jain, Transport of molecules in the tumor interstitium: a review, Cancer Res. 47 (12) (1987) 3039–3051.
[64] T.A. Bhat, R.P. Singh, Tumor angiogenesis—a potential target in cancer chemoprevention, Food Chem. Toxicol. 46 (4) (2008) 1334–1345.
[65] M.K. Gupta, R.Y. Qin, Mechanism and its regulation of tumor-induced angiogenesis, World J. Gastroenterol. 9 (6) (2003) 1144–1155.
[66] P. Danhier, G. De Preter, J. Magat, Q. Godechal, P.E. Porporato, B.F. Jordan, O. Feron, P. Sonveaux, B. Gallez, Multimodal cell tracking of a spontaneous metastasis model: comparison between MRI, electron paramagnetic resonance and bioluminescence, Contrast Media Mol. Imaging 9 (2) (2014) 143–153.
[67] M.H. Kranenborg, O.C. Boerman, J.C. Oosterwijk-Wakka, M.C. de Weijert, F.H. Corstens, E. Oosterwijk, Two-step radio-immunotargeting of renal-cell carcinoma xenografts in nude mice with anti-renal-cell-carcinoma X anti-DTPA bispecific monoclonal antibodies, Int. J. Cancer 75 (1) (1998) 74–80.
[68] K.T. Al-Jamal, Active drug targeting: lessons learned and new things to consider, Int. J. Pharm. 454 (1) (2013) 525–526.
[69] J.H. Fang, Y.H. Lai, T.L. Chiu, Y.Y. Chen, S.H. Hu, S.Y. Chen, Magnetic core-shell nanocapsules with dual-targeting capabilities and co-delivery of multiple drugs to treat brain gliomas, Adv. Healthc. Mater. 3 (8) (2014) 1250–1260.
[70] Y. Yang, K. Yu, H. Zhang, J. Dai, Z. Deng, *In vitro* assessment of the dual-targeting behavior of a peptide-based magnetic resonance imaging contrast agent, Int. J. Mol. Med. 33 (1) (2014) 215–220.
[71] J.S. Desgrosellier, D.A. Cheresh, Integrins in cancer: biological implications and therapeutic opportunities, Nat. Rev. Cancer 10 (1) (2010) 9–22.
[72] E. Blanco, C.W. Kessinger, B.D. Sumer, J. Gao, Multifunctional micellar nanomedicine for cancer therapy, Exp. Biol. Med. (Maywood) 234 (2) (2009) 123–131.
[73] J.S. Guthi, S.G. Yang, G. Huang, S. Li, C. Khemtong, C.W. Kessinger, M. Peyton, J.D. Minna, K.C. Brown, J. Gao, MRI-visible micellar nanomedicine for targeted drug delivery to lung cancer cells, Mol. Pharm. 7 (1) (2010) 32–40.